

Supporting Information

Two-dimensional transition-metal dichalcogenides-based membrane for ultrafast solvent permeation

Edison Huixiang Ang^{a,b,**} and Jia Wei Chew^{a,c,*}

^aSchool of Chemical and Biomedical Engineering, Nanyang Technological University, Singapore 637459, Singapore.

^bNatural Sciences and Science Education, National Institute of Education, Nanyang Technological University, Singapore 637616, Singapore.

^cSingapore Membrane Technology Centre, Nanyang Environmental and Water Research Institute, Nanyang Technological University, Singapore 637141, Singapore

*Corresponding author email: jchew@ntu.edu.sg (J. W. Chew)

**Co-corresponding author email: edison.ang@nie.edu.sg (E. H. Ang)

Synthesis of NiS₂ and NiAILDH nanosheets

Materials: All the materials were purchased from Sigma-Aldrich and used without further purification.

NiS₂ synthesis: In a typical NiS₂ nanosheets synthesis, nickel nitrate hexahydrate (24 mmol, Ni(NO₃)₂·6H₂O) and ethanolamine (2 mmol, EA) were dissolved in deionized water (1 mL) with 5 min sonication. Then, the solution was left undisturbed and aged for 48 h under ambient conditions. The final product Ni(OH)₂ was washed with water for several times and dried at 60 °C. Next, pure sulfur was placed at the upstream while the Ni(OH)₂ nanosheets at the downstream followed by annealing at 400 °C for 16 h under argon atmosphere. Lastly, the crystals (0.1 g) were dispersed into 100 mL of N₂-purged formamide and mechanical agitated at 500 r.p.m for 48 h. The resultant exfoliated nanosheets was collected and washed with deionized water before using for following membrane preparations.

NiAILDH synthesis: In a typical procedure, 2 mmol of $\text{NiCl}_2 \cdot 6\text{H}_2\text{O}$, 1 mmol of $\text{AlCl}_3 \cdot 6\text{H}_2\text{O}$ and 7 mmol of urea were dissolved in 200 mL of deionized water in the Teflon-lined autoclave then kept in pre-heated oven at 160 °C for 48 h. After being washed with deionized water, the as-obtained crystals was dried in oven and then calcined at 260 °C for 30 min under nitrogen atmosphere. Lastly, the crystals (0.1 g) were dispersed into 100 mL of N_2 -purged formamide and mechanical agitated at 500 r.p.m for 48 h. The resultant exfoliated naonsheets was collected and washed with deionized water before using for following membrane preparations.

S1. Thickness of NiS_2 and NiAILDH nanosheets

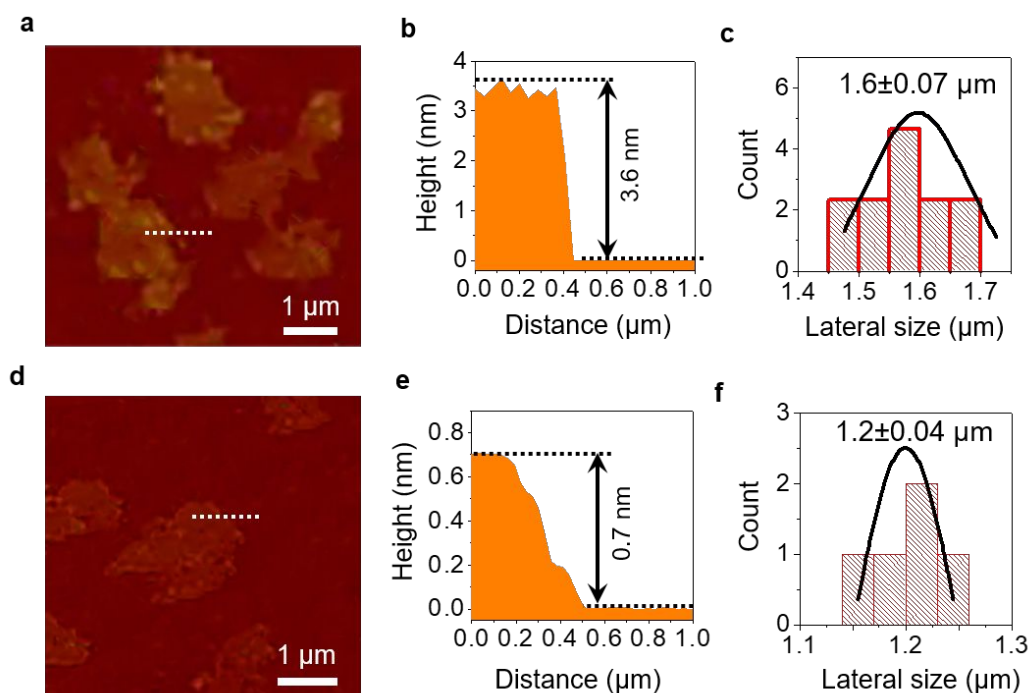


Figure S1. AFM analyses of NiS_2 and NiAILDH nanosheets. a) AFM image, b) the height profile and c) lateral size distribution (average lateral size of $1.6 \pm 0.07 \mu\text{m}$) of the NiS_2 nanosheets. d) AFM image, e) the height profile and f) lateral size distribution (average lateral size of $1.2 \pm 0.04 \mu\text{m}$) of the NiAILDH nanosheets. The thicknesses of the NiS_2 and NiAILDH nanosheets were measured with the NanoScope Analysis software.

S2. Heteroassembly of NiS_2 /NiAILDH lamellar

The heteroassembly of NiS_2 and NiAILDH lamellar was carefully evaluated by X-ray photoelectron spectroscopy (XPS), TEM, SAED and high-angle annular dark-field (HAADF) imaging. XPS experiments were carried out using a monochromated Al $K\alpha$ source (1486.7 eV) in an ultrahigh vacuum system (pressure $< 2 \times 10^{-10}$ mbar). Survey scans of NiS_2 , NiAILDH and NiS_2 /NiAILDH membranes were taken to confirm that S and O were present in the

NiS₂/NiAILDH composite (Figure S2a). The peaks at binding energies of 164.3 (S 2p) and 231.7 eV (S 2s) are attributed to the Ni-S bond in the NiS₂, while the binding energy at 530.9 eV (O 1s) corresponds to the O-H bond in the LDH. In addition, a significant shift in the binding energy of the O 1s peak (Figure S2b) for the NiS₂/NiAILDH composite (531.6 eV) with respect to the NiAILDH membrane (530.9 eV) implies the successful assembly of an anionic component with cationic LDH nanosheets.¹ The TEM images (Figures S3a-b and S3d-e) and SAED patterns (Figures S3b and S3e, insert) reveal that the monolayer NiAILDH and NiS₂ nanosheets exhibit single crystalline natures, which correspond to trigonal (Figure S3c) and cubic (Figure S3f) crystal systems, respectively. Compared with the pristine nanosheets (in Figures S3a-b and d-e displaying respectively NiAILDH and NiS₂), the HR-TEM of the hetero-assembled NiS₂/NiAILDH composite (Figure 1b; T:L ratio = 1:8; interlayer distance of 8.0 Å) exhibited two distinct contrasting regions representing the two individual nanosheets, and such alternating polycrystalline system can also be verified by the SAED pattern in Figure 1c. In addition, the HAADF image and elemental mapping of S and Al elements further confirmed that the sandwich structure was successfully formed (see Figure S3g), with the crystallographic structure of the NiS₂/NiAILDH composite (with 001 planes facing the c-axis direction) shown in Figure S3h. Furthermore, even if the lamellar was prepared with different T:L ratios (e.g., 1:1 and 1:10), the HR-TEM images, SAED patterns and elemental mapping images (see Figures S4a-f) appear similar to that of the lamellar with T:L ratio of 1:8 (Figure 1b-c and Figure S3g). Figures. S5a and S5b show the elements Al, O, Ni and S were uniformly distributed in the NiS₂/NiAILDH membrane, further confirming the successful fabrication of the NiS₂/NiAILDH hybrid, while the digital photo in Figure S5a (inset) shows that the NiS₂/NiAILDH selective layer was evenly deposited on the nylon support. In addition, Figures S5c-d display the SEM images of the cross-sections to illustrate the 2D nanostructure of the NiS₂/NiAILDH laminates deposited on the nylon support. The high-magnification AFM image (Figure S5e) shows the detailed features of the TLL membrane with a height of ~260 nm (Figure S5f), which agrees with that in Figure 1e.

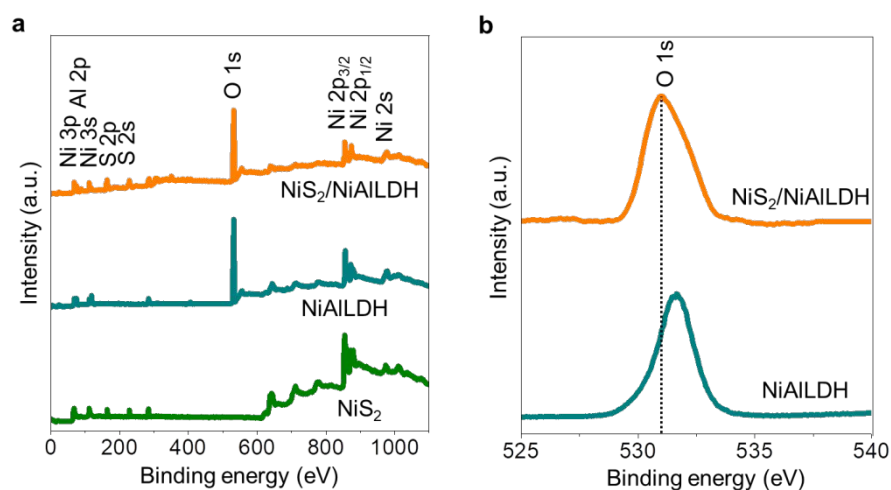


Figure S2. XPS spectra of NiS_2 , NiAILDH and $\text{NiS}_2/\text{NiAILDH}$ membranes. a) Survey scans of NiS_2 , NiAILDH and $\text{NiS}_2/\text{NiAILDH}$ membranes; b) O core level of $\text{NiS}_2/\text{NiAILDH}$ membrane in comparison with NiAILDH membrane.

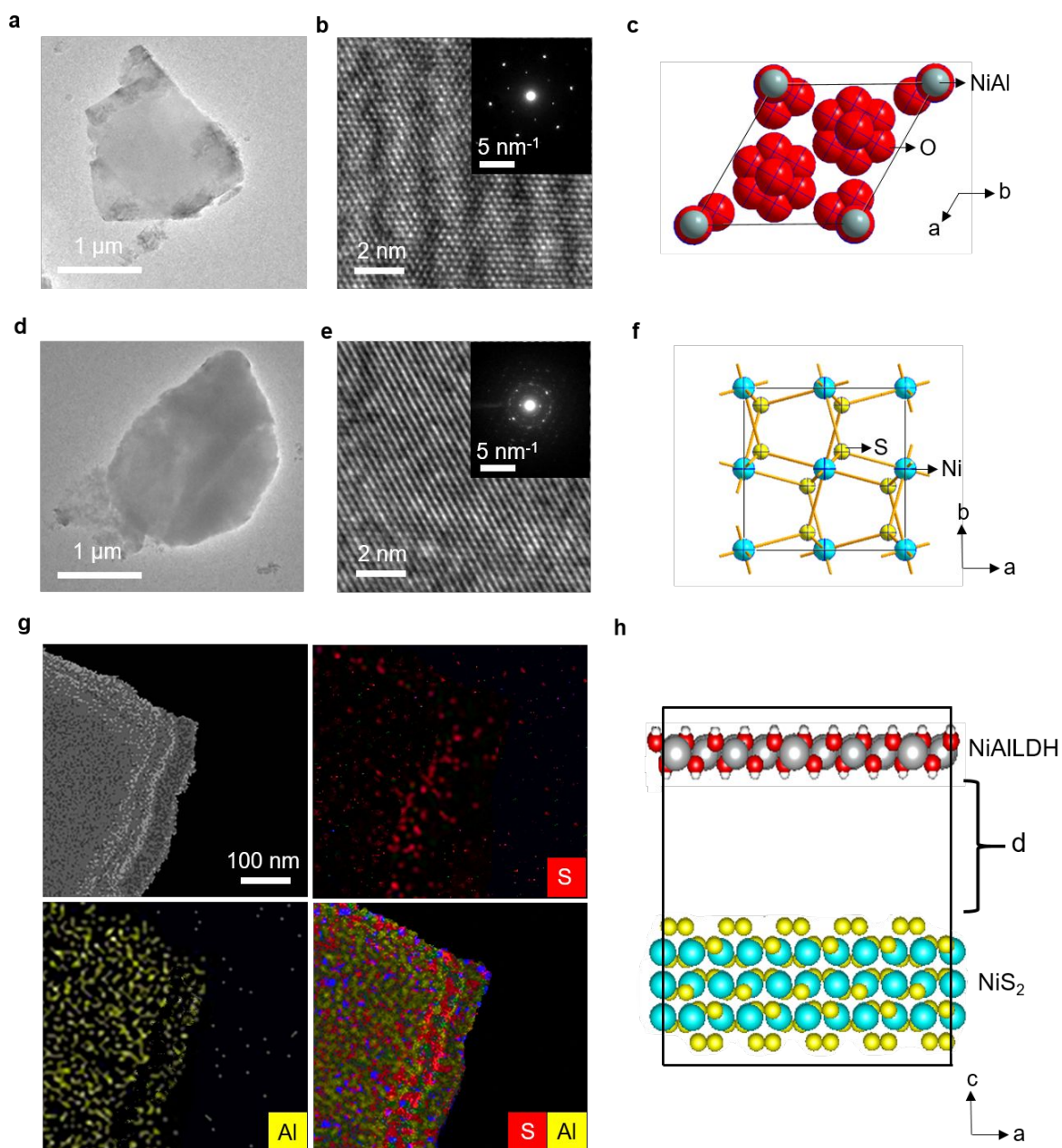


Figure S3. Characterization of single layer NiS_2 and NiAILDH nanosheets with comparison to the hetero-assembled $\text{NiS}_2/\text{NiAILDH}$ hybrid. a) TEM image of NiAILDH nanosheets and its corresponding b) HR-TEM image (insert: SAED pattern) and c) crystallographic structure. d) TEM image of NiS_2 nanosheets and e) its corresponding HR-TEM image (insert: SAED pattern) and f) crystallographic structure. g) HAADF image of $\text{NiS}_2/\text{NiAILDH}$ composite (T:L ratio = 1:8 with interlayer spacing of 8.0 Å) and its corresponding elemental mapping images of S, Al, and S/Al, as well as its h) composite crystallographic structure of NiAILDH and NiS_2 layer with tunable interlayer distance, d.

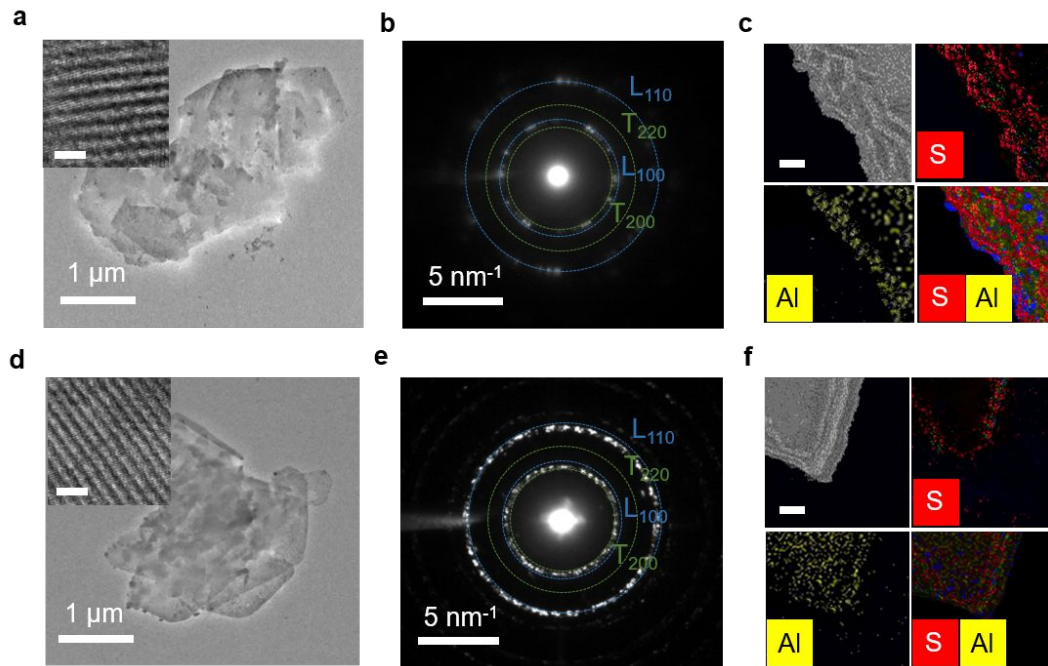


Figure S4. Characterization of $\text{NiS}_2/\text{NiAILDH}$ composites with two different T:L ratios. a) TEM image of $\text{NiS}_2/\text{NiAILDH}$ composite with T:L ratio of 1:1 (corresponds to interlayer distance of 8.7 Å) and its insert HR-TEM image (scale bar: 2 nm), as well as its b) SAED pattern and c) HAADF top-view image (scale bar: 100 nm) and elemental mapping images. d) TEM image of $\text{NiS}_2/\text{NiAILDH}$ composite with T:L ratio of 1:10 (corresponds to interlayer distance of 8.3 Å) and its insert HR-TEM image (scale bar: 2 nm), as well as its e) SAED pattern and f) HAADF top-view image (scale bar: 100 nm) and elemental mapping images.

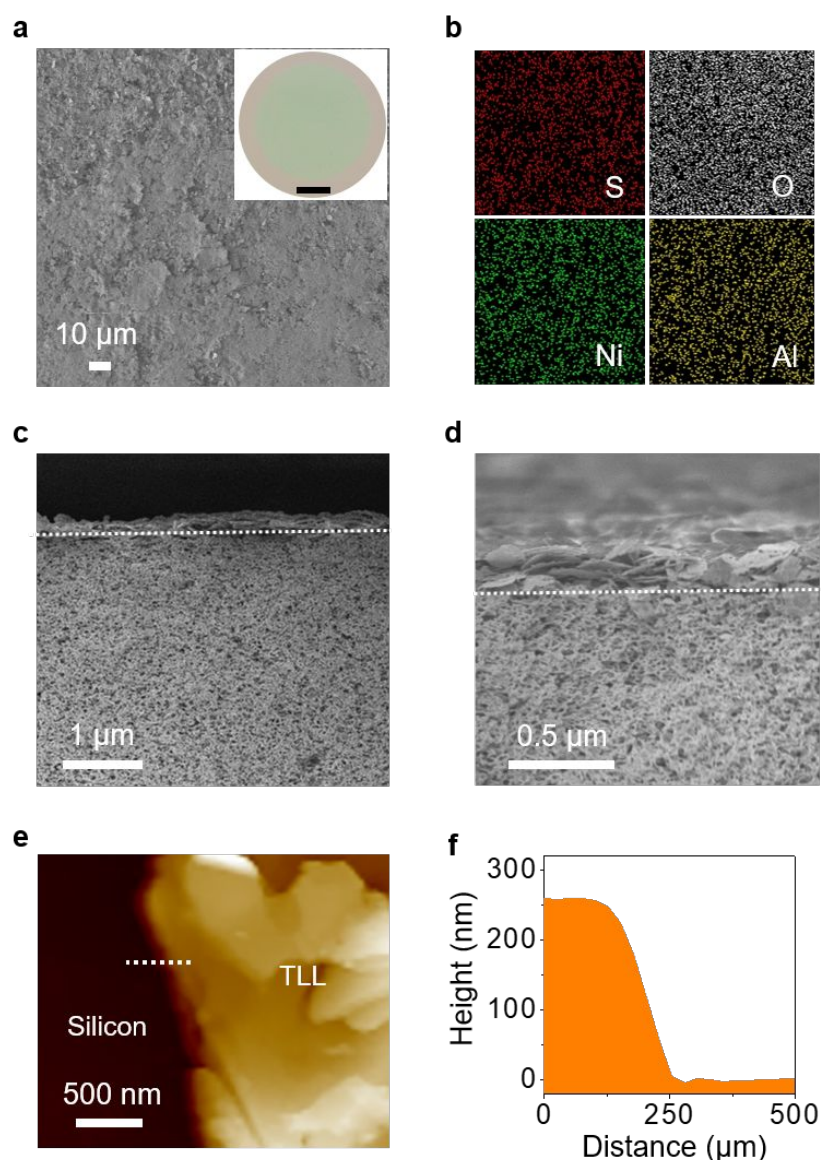


Figure S5. Elemental distribution of the $\text{NiS}_2/\text{NiAILDH}$ membrane. a) SEM image, inset: photograph of $\text{NiS}_2/\text{NiAILDH}$ (T:L = 1:8) membrane on nylon with a scale bar of 1 cm and b) its corresponding elemental mapping images. The elemental distribution of Al, O, Ni and S in the $\text{NiS}_2/\text{NiAILDH}$ membrane was measured using the field emission scanning electron microscopy (FESEM) equipped with Oxford energy-dispersive X-ray spectroscopy (EDX). c) low-magnification SEM image and d) high-magnification SEM image of the cross-section of the $\text{NiS}_2/\text{NiAILDH}$ laminate on the nylon support, with the dotted lines demarcating the 2D laminates from the nylon substrate. e) High-magnification AFM image of TLL membrane on silicon substrate and f) its corresponding height profile.

S3. Filtration performance

The air-pressurized filtration module (see Figure S6a) consisted of a digital pressure gauge (P), feed tank capacity of 4 l, filtration unit with stirring mechanism on the feed side to mitigate concentration polarization, and weighing balance (WB) to measure the amount of permeate accumulated per unit time. In this study, a porous stainless steel disk (see Figure S6a(3)) provided the membrane with excellent mechanical support of up to 5 bars (Figure 2d); to improve the mechanical strength of the membrane for practical applications, the nanosheets can be embedded into the cross-linked polymeric network.²

This customized set-up was used to examine the separation performance of the membranes. For the evaluation of the membrane separation efficacies, various organic dyes, namely, methyl orange (MO), acid fuchsin (AF) and brilliant blue G (BB), were examined and the photographs (Figure S6b) show that after filtration, the permeate solutions were clear with reference to their respective feed solutions before filtration. Further investigation of the separation test was verified by UV-vis spectrophotometer (Figure S6c-e). Based on mass balance (i.e., feed solute mass = retentate solute mass + permeate solute mass) and adsorption $(V_F C_F - V_R C_R - V_P C_P) / V_F C_F \times 100\%$, where C_F , C_P and C_R are the concentrations of the feed, permeate, and retentate solution respectively, and V_F , V_P , and V_R are the feed, permeate and retentate volumes of 150, 120 and 30 mL, respectively) considerations, the results derived from the UV-vis spectra indicate negligible adsorption, which implies that most dye molecules were rejected rather than entrapped in the membranes.

The chemical structures and molecular sizes of the organic solutes solvated with acetone are summarized in Table S1. The probe solutes were first generated using ChemDraw Ultra version 13.0 and then the energy minimization was performed using the MM2 method. Subsequently, we estimated the dimensions and molecular volumes of the solutes by using Connolly accessible solvent surface method.³ Nano Measurer versions 1.2 was used to estimate the dimensions of the solvated solute, while the Materials Studio 8.0 software was used to estimate the molecular volumes of the probe solutes.

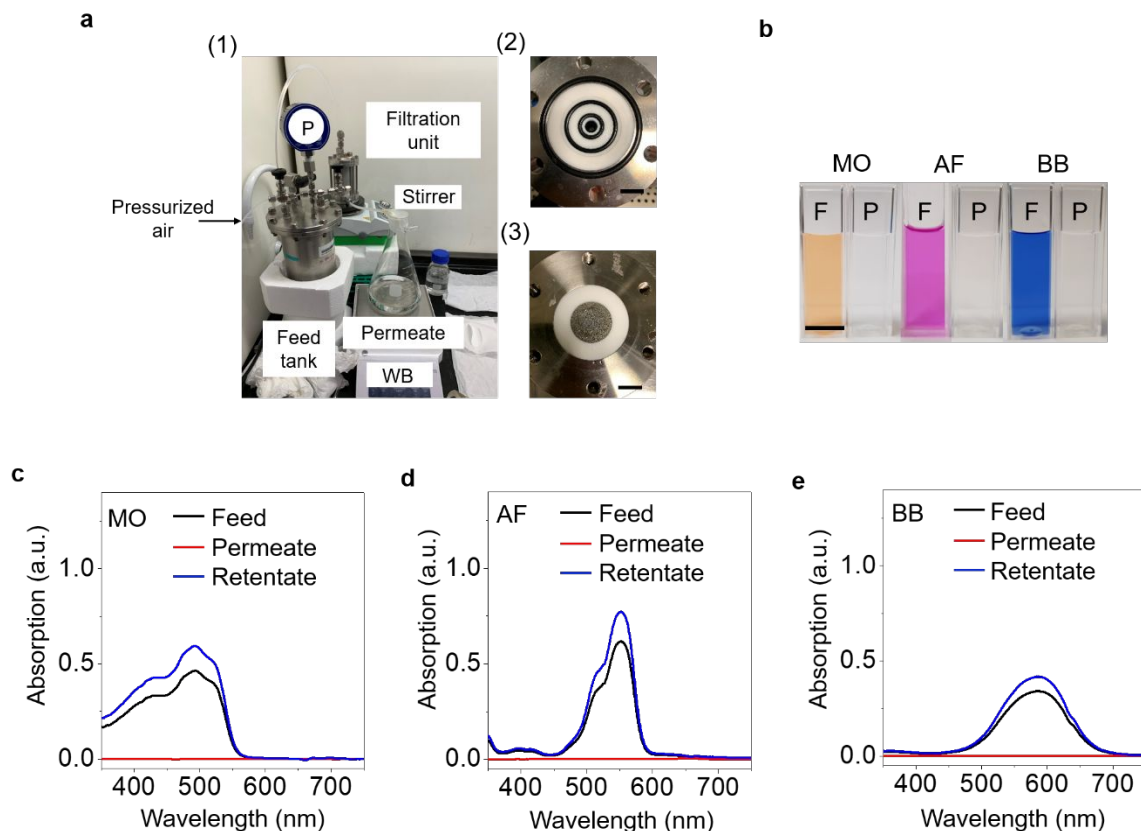
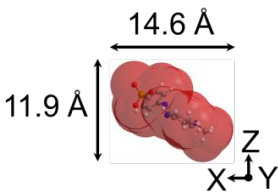
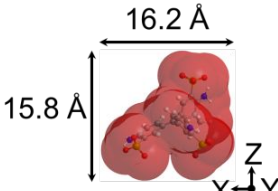
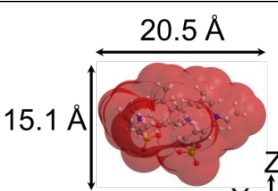


Figure S6. Filtration performance. a) (1) Customized dead-end filtration setup, with Teflon internally and stainless steel externally. P denotes digital pressure gauge and WB denotes weighing balance; (2) cross-section of feed configuration consisting of O-rings. Membranes were secured by the O-rings to prevent leakage during the separation tests; (3) cross-section of permeate configuration consisting of a porous (~400 nm pore size) stainless steel disk to provide mechanical support to the membrane for high-pressure filtration tests. b) Photographs (scale bar: 1 cm) of feed (F) and permeate (P) solutions containing different dye molecules in acetone before and after filtration. UV-vis absorption spectra of the feed, permeate and retentate solutions for c) methyl orange (MO); d) acid fuchsin (AF); and e) brilliant blue G (BB) in acetone (color coded).

Table S1. Chemical structure and molecular size of various organic solutes

Name	Dimensions of organic solute (Å)	Molecular weight (g mol ⁻¹)	Occupied Volume (Å ³)
Methyl orange (MO)		327	859
Acid fuchsin (AF)		586	1188
Brilliant blue G (BB)		858	1951

S4. Stability of the TMD/LDH lamellar (TLL) membranes

To study the stability of the TLL membranes in an organic solvent, we firstly passed MO/water and MO/acetone solutions through NiS₂/NiAlLDH, MoS₂/NiAlLDH and WS₂/NiAlLDH membranes. Figures. S7a-b show that the permeances attained steady-state after about 30 min, and both permeance and rejection values remained approximately the same for at the end of 12 hours of filtration, indicating that the membranes have excellent separation stability even in the organic solvent. These filtration tests were performed using an air-pressurized dead-end module (Figure S6a), operating at 1 bar with 500 r.p.m mechanical stirring. Moreover, we demonstrated that the TLL membranes remain intact after soaking in the water and organic solvents for 7 days (Figure S8). Further investigation was performed on the wetted films using XRD analyses (Figures S9a-f). As is well-known, the XRD intensity can be correlated with the thickness of the selective layer (see Table S2), while the 2θ position can be attributed to the interlayer distance. Therefore, no distinct change in the XRD intensities and 2θ positions implies negligible swelling of membranes after a week. The stability of the TLL membranes in both the water and acetone solvents could be attributed to the electrostatic interaction between the anionic TMDs and cationic LDH nanosheets.

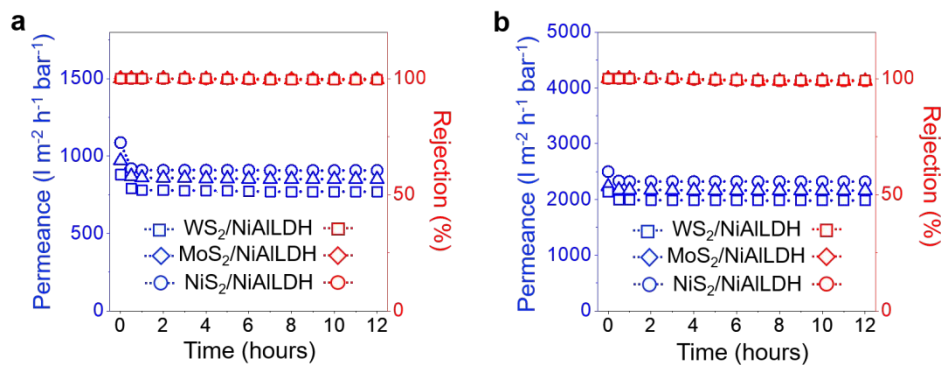


Figure S7. Durability test of TLL membranes. Separation of a) MO/water solution and b) MO/acetone solution through 250 ± 20 nm thick $\text{NiS}_2/\text{NiAILDH}$, $\text{MoS}_2/\text{NiAILDH}$ and $\text{WS}_2/\text{NiAILDH}$ membranes; permeances represented by blue and rejection represented by red.

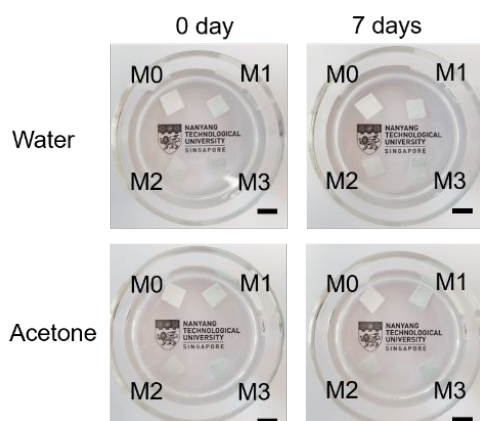


Figure S8. Stability test of TLL membranes. Photographs show bare nylon support (M0) and nylon supported with 250 ± 20 nm thick $\text{NiS}_2/\text{NiAILDH}$ (M1), $\text{MoS}_2/\text{NiAILDH}$ (M2), and $\text{WS}_2/\text{NiAILDH}$ (M3) membranes immersed in pure water and acetone solvents for 0 day and 7 days; scale bar represents 15 mm.

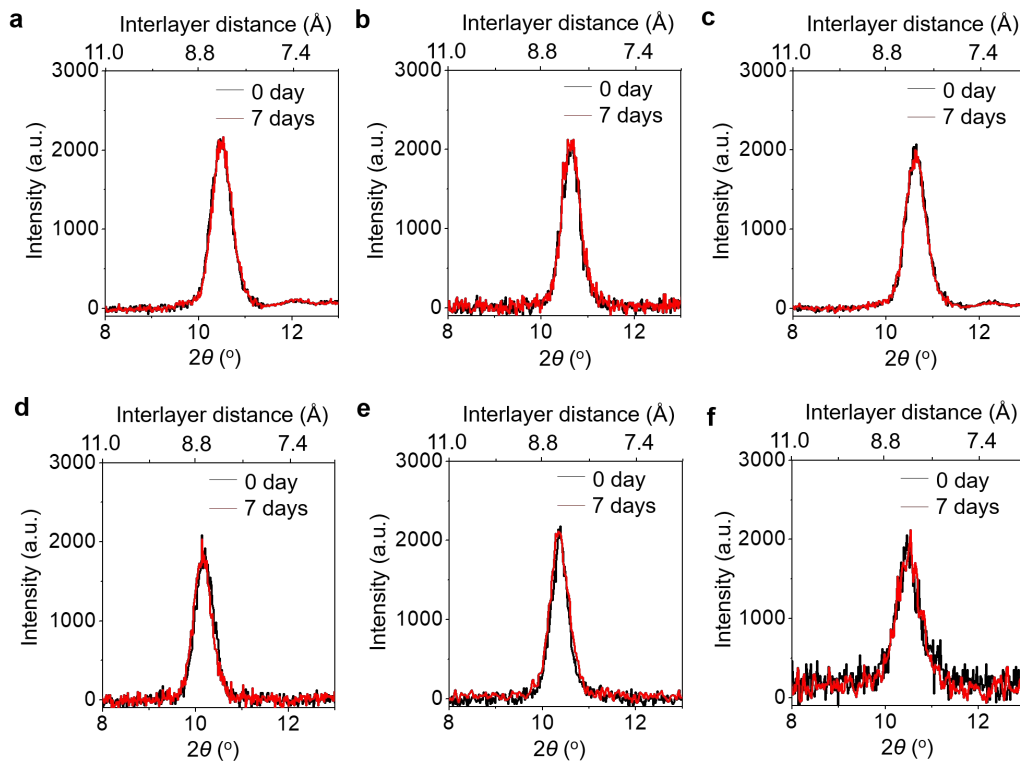


Figure S9. XRD patterns of wetted laminates (250 ± 20 nm thick) in pure water and acetone solvents for 0 day and 7 days. XRD patterns of a) $\text{NiS}_2/\text{NiAILDH}$; b) $\text{MoS}_2/\text{NiAILDH}$; c) $\text{WS}_2/\text{NiAILDH}$ laminates wetted with acetone and d) $\text{NiS}_2/\text{NiAILDH}$; e) $\text{MoS}_2/\text{NiAILDH}$; f) $\text{WS}_2/\text{NiAILDH}$ laminates wetted with water.

Table S2. XRD intensities of $\text{NiS}_2/\text{NiAILDH}$ laminates of various thicknesses estimated from AFM measurements.

XRD intensity (a.u.)	AFM measurement (nm)
1381 ± 33	95 ± 5
1789 ± 45	149 ± 19
2087 ± 49	250 ± 20
2701 ± 58	612 ± 34
3139 ± 62	1205 ± 48

S5. OSN performance comparison

To further demonstrate the excellent OSN performance of the TLL (TMDs/LDH Lamellar) membranes, we compared them with commercial and other advanced membranes including one of the emerging 2D graphene-based membranes (Figure S10). The frequently studied methyl orange (MO) in acetone was chosen as the solute for the comparison. Figure S10 reveals the typical trade-off between acetone permeance and rejection reported for several OSN membranes (in the blue colored region). Compared with the commercial polymeric membrane (i.e., Integrally Skinned Asymmetric (ISA)), TLL membranes exhibited permeances of 3 orders-of-magnitude greater and a rejection of $\sim 100\%$ for a small solute whose molecular weight is only 327 g mol^{-1} . It should also be noted that the highest reported acetone permeance at $15 \text{ l m}^{-2} \text{ h}^{-1} \text{ bar}^{-1}$ by the mixed matrix membrane (MMM) had a rejection of only 90% , while the-state-of-the-art graphene-based membrane (GBM) had an acetone permeance of $13 \text{ l m}^{-2} \text{ h}^{-1} \text{ bar}^{-1}$. On the contrary, as listed in Table S3, our TLL membranes exhibited acetone permeance of 2–3 orders-of-magnitude higher than that of existing membranes, along with excellent rejection of close to 100% , at a much lower operating pressure and thereby much lower energy requirement. Such superior separation performances at low operating pressure (which means low energy consumption) of our TLL membranes makes it promising for OSN membrane technology.

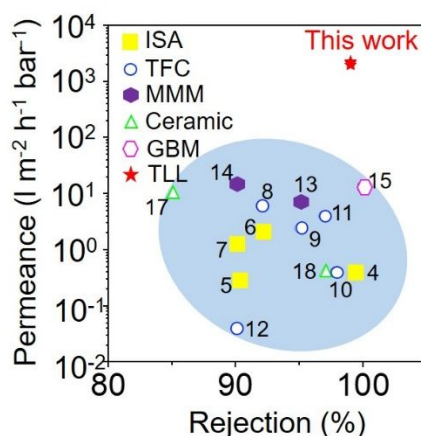


Figure S10. Comparison of TMDs/LDH membranes performances with the existing reported OSN membranes. Permeance as a function of rejection for several solute molecules taken from literature is plotted together with the data obtained from the TMDs/LDH membranes. All data points in the blue colored regions are obtained from Ref. [4-17]. ISA, TFC, MMM, GBM and TLL stand respectively for Integrally Skinned Asymmetric, Thin Film Composite, Mixed Matrix Membranes, Graphene-Based Membranes and TMDs/LDH Lamellar membranes.

Table S3. Comparison of the separation performances with various membranes.

Category	Membrane	ΔP (bar)	Permeance ($\text{l m}^{-2} \text{ h}^{-1} \text{ bar}^{-1}$)	Solute in acetone/ Rejection (%)	Ref.
ISA	DuraMem 150 (Commercial membrane)	30	0.3	Styrene oligomers/99	4
	Cross-linked P84 PI	300	0.3	Styrene oligomers/90	5
	PEEK	30	2.2	Styrene oligomers/92	6
	PAI	5	1.2	Styrene oligomers/90	7
TFC	PA/PAN	13.8	6	Oleic acid/92	8
	PA/cross-linked P84 PI	30	2.4	Styrene oligomers/95	9
	PAR-RES/PI	30	0.4	Styrene oligomers/97.8	10
	(PIM-1)/ PEI/PAN	20	4	Sudan II/96.9	11
	(PS-b- PEO/PAA)/ alumina	40	0.04	Polyethylene glycols/90	12
MMM	APTMS/PI	30	7.5	Styrene oligomers/95	13
	MOF HKUST-1	10	15	Styrene oligomers/90	14
GBM	DPAN/PEI-GO	10	13	Polyethylene glycol/~100	15
Ceramic	Inopor TiO ₂ /alumina	10	0.4	Erythrosine B/97	16
	Grignard grafted TiO ₂ /alumina	10	10	Styrene oligomers/85	17
TLL	NiS ₂ /NiAILDH	1	2319	MO/99.9	This work
	MoS ₂ /NiAILDH	1	2118	MO/99.6	
	WS ₂ /NiAILDH	1	1980	MO/99.5	

S6. Water desalination of TLL membrane

We also tested the feasibility of our NiS₂/NiAILDH membrane for desalination by quantifying the salt concentration using an ion conductivity meter. The NiS₂/NiAILDH membrane exhibited 7-fold and 3-fold improvements in salt rejection as compared to the pristine NiS₂ and NiAILDH, respectively, while providing a superior water permeance of 902 l m⁻² h⁻¹ bar⁻¹ (Figure S11a). The significant increase of rejection could be attributed to the packing efficiency of the laminate. Moreover, the NiS₂/NiAILDH membrane was also able to reject various types of salts with rejection of 28-45% (Figure S11b), which is on par with reported 2D material-based membranes.^{18,19}

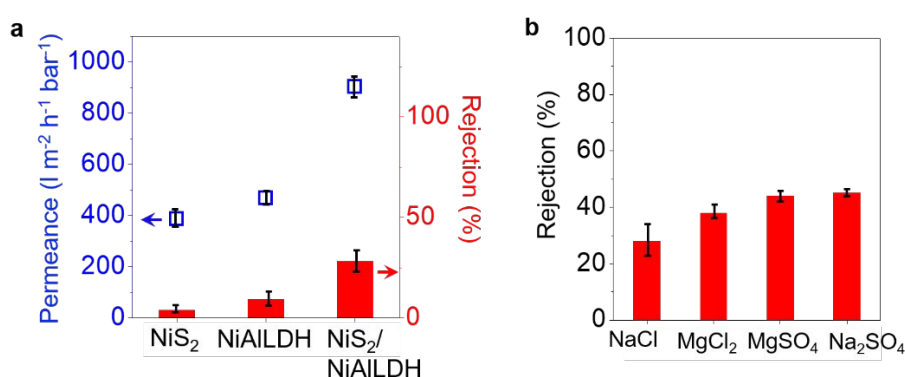


Figure S11. Water desalination of the TLL membrane. a) Permeance and rejection of NaCl salt in water through 600 ± 55 nm-thick NiS₂ and NiAILDH membranes, in comparison with 250 ± 20 nm-thick NiS₂/NiAILDH membranes. b) Rejection of various salts in water through 250 ± 20 nm-thick NiS₂/NiAILDH membranes.

S7. Photo-assisted OSN membrane

For the purification of pharmaceuticals using OSN technology, membrane fouling due to the accumulation of organic foulants is inevitable, which reduces permeability and increases energy cost. Herein, we present an innovative strategy of using photo-assisted nanofiltration to degrade and mineralize the organic foulants on the OSN membrane. The photo-assisted nanofiltration can be viewed in Movie S1. To study the antifouling property of the photo-assisted OSN membrane, we first filtered pure acetone (Ace) solvent through the membrane, followed by introducing the brilliant blue G in acetone (BB/Ace) solution to foul the membrane, after which we washed the fouled OSN membrane with water in the absence of light

illumination (control experiment; Figure S12a) and in the presence of light illumination (Figure S12b), and finally, the membrane was used for filtering pure acetone solvent again. The permeance results were used to evaluate the permeance recovery percentage (*PRP*), which was calculated by:

$$PRP(\%) = \frac{P_{S,n}}{P_{S,1}}$$

where $P_{S,1}$ is the initial permeance of the pure acetone solvent before filtering the BB/Ace solution and $P_{S,n}$ is the final permeance after photo-assisted cleaning of the fouled OSN membrane using a solar simulator and water. Figure S12a versus Figure S12b clearly shows that there was a distinct increment of permeance as a function of filtration time during photo-assisted cleaning when compared to the control experiment (without light illumination). As a result, the former yielded a *PRP* of 99% after photo-assisted cleaning using water. With reference to the bare NiS₂/NiAILDH membrane (Figure S12c, (1)), the color of the fouled membrane changed from dark blue (Figure S12c, (2)) to light blue (Figure S12c, (3)), further confirming the successful photo-degradation of the organic foulants. This study therefore reveals that the unique strategy of using photo-assisted cleaning of fouled OSN membrane for enhanced performance and energy-efficiency is feasible. This is promising for the fabrication of next-generation photo-assisted OSN membranes.

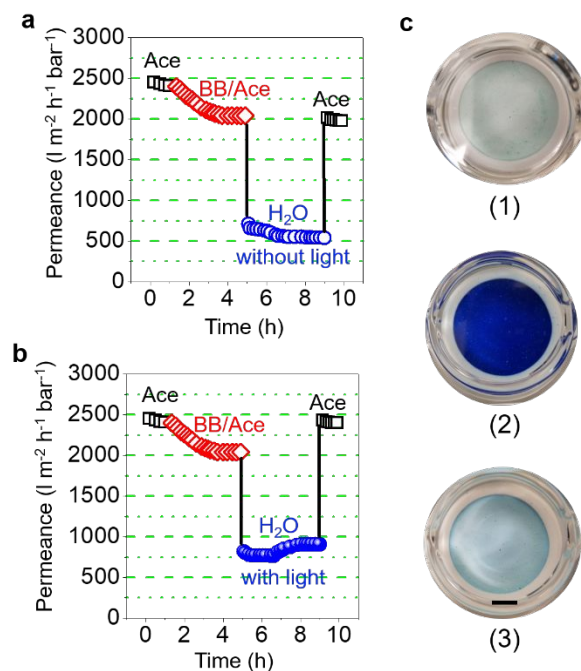


Figure S12. Photo-assisted cleaning of NiS₂/NiAILDH membrane. a) Control experiment: continuous operation of OSN through NiS₂/NiAILDH membranes, and then clean with pure water without light illumination. b) The continuous operation of OSN through NiS₂/NiAILDH membranes and then clean with pure water with light illumination. c) Photographs of the bare NiS₂/NiAILDH membrane (1); cleaning fouled membrane using water without light illumination (2); and after photo-assisted cleaning of membrane using water (3); inset: scale bar represents 1 cm.

S8. Heteroassembly of TMDs/LDH lamellar with reduced interlayer distance for OSN

Positively charged spacers such as polycation¹⁸ and multivalent cation²⁰ have been previously used to control the interlayer spacing of the anionic 2D lamellar membrane for enhanced molecular separation. Herein, we propose that similar cationic 2D LDH-regulated anionic 2D TMD assembly could improve the packing efficiency of the lamellar structure, which would reduce the interlayer distance for better rejection of smaller solutes. Such a unique strategy would also result in a thin selective layer that would boost the solvent permeability, as shown in Figure 2c. We chose NiAILDH as a cationic spacer because Ni-based materials are well-known to be stable in harsh organic solvents²¹ and robust in long-term nanofiltration operation.²²

The cationic NiAILDH nanosheets were added into the anionic TMDs (i.e. NiS₂, MoS₂, or WS₂) suspension with their respective appropriate mass ratio for heteroassembly. The mass ratio for the heteroassembly of TMDs (T) and LDH (L) is the ratio of the molar mass of TMDs

(i.e. NiS_2 , 122.8 g mol^{-1}) divided by its in-plane unit cell area to the molar mass of LDH (i.e. NiAlLDH , 294.0 g mol^{-1}) divided by its in-plane unit cell area. The in-plane unit cell area was calculated using the equation $a \times b \times \sin 120^\circ$, where a and b are the lattice parameters of the unit cell. Since the NiS_2 (space group of $\text{Pa}\bar{3}$) has the lattice parameters of $a = b = 0.56 \text{ nm}$ and the NiAlLDH (space group of $\text{R}\bar{3}\text{m}$) has $a = b = 0.31 \text{ nm}$, the in-plane unit cell areas for NiS_2 and NiAlLDH are 0.27 nm^2 and 0.083 nm^2 , respectively. In addition, since the zeta potential values of NiS_2 and NiAlLDH were close to each other, the attained heteroassembled $\text{NiS}_2/\text{NiAlLDH}$ composite exhibited charge neutrality (as verified using zeta potential measurement) when the T:L mass ratio was 1:8. For the heteroassembled $\text{MoS}_2/\text{NiAlLDH}$ and $\text{WS}_2/\text{NiAlLDH}$ composites, charge neutrality (as confirmed by zeta potential measurement) was achieved when the T:L mass ratios were respectively $\sim 1:2$ and $\sim 1:1$. These measured zeta potential values are approximately zero, which means minimum electrostatic repulsive forces between the two oppositely charged components that leads to smaller interlayer distances (see Figure 3a). On the other hand, any deviation of the $\text{NiS}_2:\text{NiAlLDH}$ mass ratio from 1:8 would generate excess charges that will increase either the negatively charged (i.e. T:L mass ratio of 1:1 gave -25 mV) or positively charged (i.e. T:L mass ratio of 1:10 gave $+29 \text{ mV}$) constituents, and thus result in increased interlayer distance. The cationic LDH and anionic TMDs was mixed homogenously using a mechanical stirrer for 1 h followed by vacuum-filtration on the nylon support while stirring to prevent aggregation of nanosheets. Plausibly, the compressive force (indicated by blue arrows in Figure S13) arising from vacuum-filtration packed the nanosheets into laminates, and the introduction of cationic LDH into the anionic TMD suspension customized the assembly of oppositely charged nanosheets alternately by electrostatic attraction (indicated by purple arrow in Figure S13b). Specifically, after introducing the cationic LDH into the TMD lamellar, the heteroassembly of the TMD/LDH lamellar decreased the interlayer distance (d), thereby allowing smaller solvent molecules to pass through while blocking the larger solute molecules. As illustrated in Figures S13a and S13b, the combination of both electrostatic interaction and compressive force improved the packing efficiency (i.e., narrowed the interlayer distance, d) of the laminate, and thus increased the rejection of smaller solutes; also, the hetero-film provided a shorter transportation pathway for fast solvent permeation due to the compact and thin membrane thickness (Δx) derived from hetero-assembly.

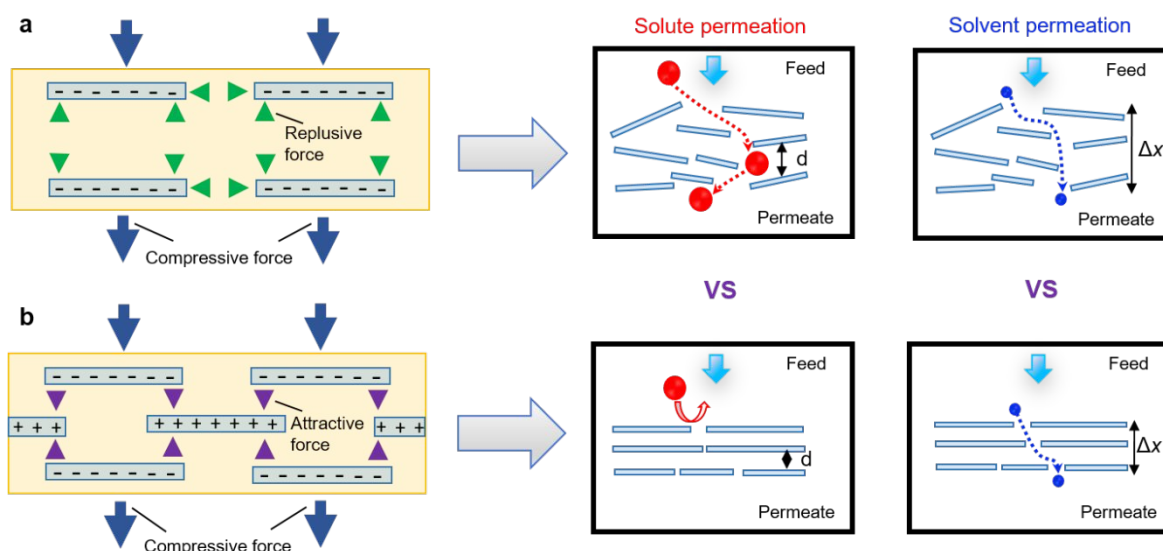


Figure S13. Schematic showing the assembly of the TMD/LDH lamellar. Assembly of anionic TMDs in the a) absence of cationic LDH nanosheets, and b) presence of cationic LDH nanosheets.

S9. Solvent permeation experiments

To understand the permeation rates of organic solvents filtering through the $\text{NiS}_2/\text{NiAlLDH}$ membranes, we have performed air-pressurized dead-end filtration measurements. In the solvent permeation experiment, the volume of permeate collected was monitored over up to 8 h (Figure S14), and then divided by the effective area of the membrane and pressure drop across the membrane to obtain the permeance with unit of $\text{l m}^{-2} \text{h}^{-1} \text{bar}^{-1}$. The permeation rates through the $\text{NiS}_2/\text{NiAlLDH}$ membranes with interlayer distances of 8.0, 8.3, and 8.7 Å were evaluated to give acetone permeances of 2464, 2737 and 3286 $\text{l m}^{-2} \text{h}^{-1} \text{bar}^{-1}$, respectively.

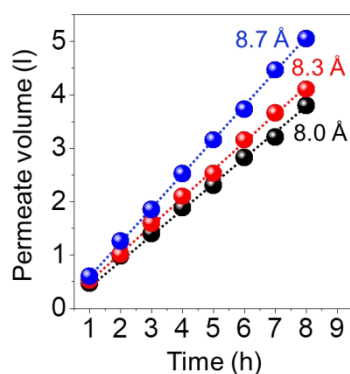


Figure S14. Acetone permeation through $\text{NiS}_2/\text{NiAlLDH}$ membranes. Permeate volume plotted against time for $\text{NiS}_2/\text{NiAlLDH}$ membranes with different interlayer distances.

Comparison with Hagen-Poiseuille flow equation

Based on the Hagen-Poiseuille equation with no-slip boundary conditions,²³ we estimated the acetone permeation rate through NiS₂/NiAILDH membranes. Acetone flow through a slit geometry can be described by

$$Permeance \approx \frac{h^4 \Delta P}{12L^2 \eta \Delta x}$$

where h is the interlayer distance (8.0 Å), ΔP (1 bar) is the pressure gradient, L is the average lateral length of the nanosheets (1.4 μm), η is the viscosity of acetone (3.2×10⁻⁴ Pa.s at 20 °C) and Δx is the thickness of membrane (250 nm). For the 250 nm-thick membrane, this equation yields a permeance of ~4×10⁻⁴ l m⁻² h⁻¹ bar⁻¹, which is 6 orders-of-magnitude lower than the experimental values.

S10. Solute permeation experiments

The solute permeation experimental setup (shown in Figure S15a) consisted of mainly two compartments, namely, feed and permeate compartments. The membrane was sandwiched between these two compartments, with the feed side filled with the probing solution and both compartments agitated with magnetic stirrers to minimize concentration polarization, as shown in the inset of Figure S15b. The organic solute permeation through the NiS₂/NiAILDH membrane was examined as a function of time. Figure S15b shows that MO permeation was expectedly dependent on the thickness of the membrane. For the 2D material-based membrane, the membrane thickness can easily be manipulated by changing the concentration of the constituents added during membrane fabrication. Based on the slope in Figure S15b, we can determine the molar flux (J) of the solute (namely, MO) at a given feed concentration. As shown in Figure S15c, the molar flux decreased exponentially with membrane thickness (Δx), affirming that the molar flux of the solute is dependent on the membrane thickness. According to Fick's law of diffusion,²⁴ for a plot of J versus $1/\Delta x$ (Figure S15d), the slope divided by the concentration difference between feed and permeate gives the diffusion coefficient (D). Figure S16 shows that the diffusion coefficient D changes with interlayer distance, with larger interlayer distances expectedly exhibiting higher D values. In addition, solutes with higher molar volumes tended to exhibit smaller D values. These observations are in accordance with the trends for previously reported systems using salt ions as the permeated solute.²⁵

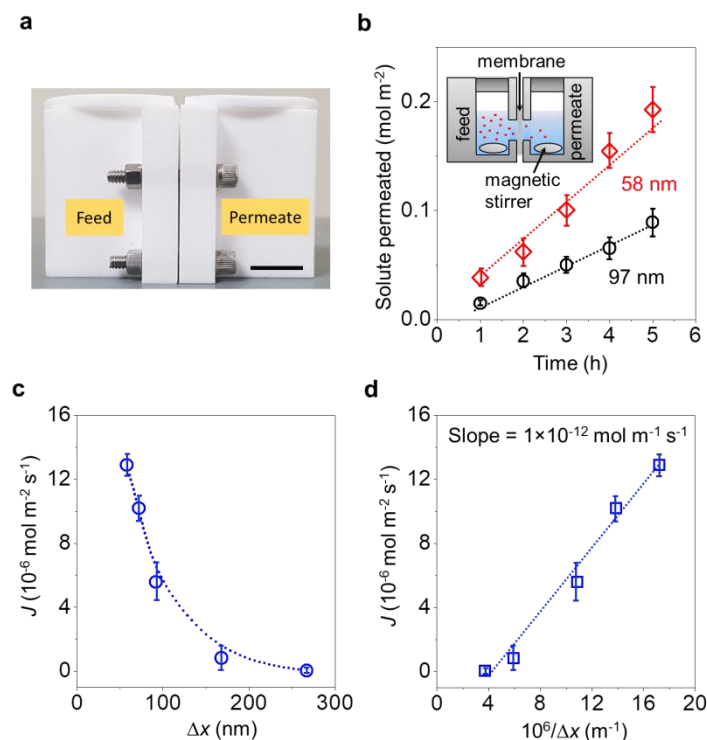


Figure S15. Solute permeation through various membrane thicknesses. a) Photograph of the membrane-filtration apparatus made of Teflon which consisted of feed and permeate compartments; scale bar denotes 2 cm. b) Permeation of MO solute through the NiS₂/NiAII LDH membranes (with interlayer spacing of 8.0 Å) of thicknesses of 58 nm versus 98 nm; inset shows the membrane sandwiched between feed and permeate compartments, and magnetic stirrers in both compartments to ensure homogenous stirring to minimize concentration polarization. c) Dependence of molar flux (J) of MO solute in acetone solvent on membrane thickness. d) The effect of membrane thickness on the steady-state flux of MO solute; the diffusion coefficient (D), calculated using the slope (specified in inset: $1 \times 10^{-12} \text{ mol m}^{-1} \text{ s}^{-1}$) divided by concentration difference between feed and permeate (in this case, $7.95 \times 10^{-4} \text{ mol m}^{-3}$), was $12.5 \times 10^{-10} \text{ m}^2 \text{ s}^{-1}$.

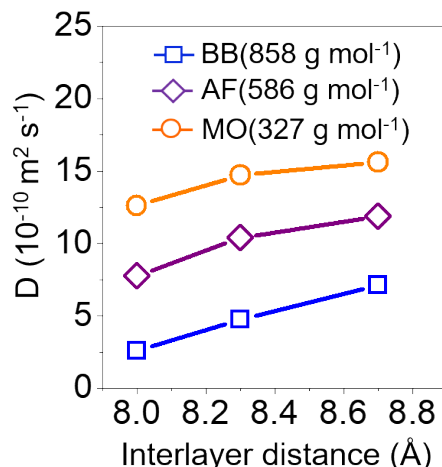


Figure S16. Organic solute diffusion through different interlayer distances. The diffusion coefficient of MO, AF and BB solutes in acetone for interlayer distance ranging from 8.0 Å to 8.7 Å.

Comparison with Wilke and Chang flow equation

The diffusion coefficient (D) is associated with solute radius and temperature of the solution in a specified solvent. The theoretical D can be calculated by Wilke and Chang flow equation,²⁶ which can give satisfactory predictions of the diffusivity of trace organic solutes in organic solvents:

$$D = \frac{1.173 \times 10^{-13} (\phi M)^{0.5} T}{\mu V_m^{0.6}}$$

where ϕ is the association factor for the solvent ($\phi = 1.0$ for acetone), M is the molecular mass of the solvent ($M = 58 \text{ g mol}^{-1}$), T is the temperature of the solution, μ is the viscosity of the solvent (0.32 mN s m^{-2}), and V_m can be estimated from the group contributions to molar volume of the organic solute. This equation yields D values ranging from 10^{-9} to $10^{-10} \text{ m}^2 \text{ s}^{-1}$ for MO, AF and BB solutes in acetone solvent at a temperature range between 20 - 40 °C. These theoretical D values are of similar order-of-magnitude to that of the experimental results (Figure S16).

S11. Arrhenius characteristics of solute diffusion

Finally, to completely exclude the diffusion contribution on the experimentally observed solute permeation, we tabulated the diffusion activation energies (E_a) of various solutes with varying molecular sizes for interlayer distances of 8.0, 8.3 and 8.7 Å by measuring their diffusion coefficients at different temperatures (T). The relationships between diffusion and temperature for solutes of different molecule sizes and different interlayer distances are displayed respectively in Figures. S17a and S17b, from which the activation energy (E_a) can be extracted. The E_a values for the MO, AF and BB solutes permeating through the interlayer distance of 8.0 Å were 7.9, 15.5, and 37.0 kJ mol⁻¹, respectively; and the E_a values for the MO solute diffusing through interlayer distances of 8.3 and 8.7 Å were 4.0 and 3.7 kJ mol⁻¹, respectively. The E_a value (~2.5 kJ mol⁻¹) was relatively unchanged for different molecular sizes of solutes in bulk acetone solvent (Figure S18), while the measured E_a values in the presence of membrane showed significant changes with solute sizes and membrane interlayer distances. These observations are in agreement with the previously reported systems using salt as solute permeating through graphene layers.¹⁹

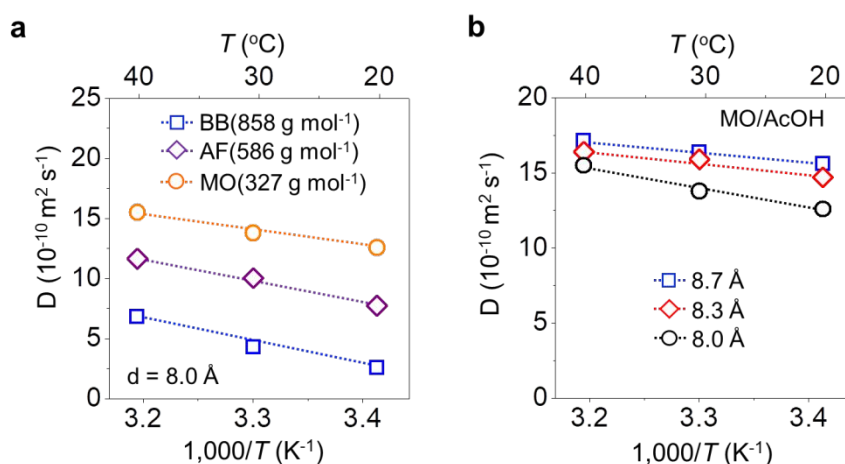


Figure S17. Arrhenius plots for the $\text{NiS}_2/\text{NiAILDH}$ membrane. Temperature dependence of the diffusion coefficient for a) solutes of different sizes in acetone solvent for a fixed interlayer distance of $d = 8.0$ Å; and b) membranes with different interlayer distances for MO dissolved in acetone solvent.

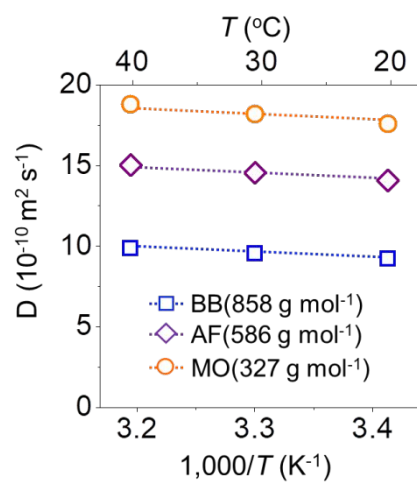


Figure S18. Arrhenius plots of organic dye diffusion through the bulk solvent. The diffusion coefficients of various solutes in acetone solvent versus the temperature of the solution. The D values were obtained from the Wilke and Chang flow equation in Section S10.

S12. Solute permeation mechanism

Based on the Wijmans *et al.* solution-diffusion and pore-flow models, solution-diffusion and/or size-exclusion mechanisms can be observed in nanofiltration membranes.²⁷ To understand the underlying mechanism of solute permeation through the NiS₂/NiAILDH membrane, we have conducted permeation rate and rejection tests at various feed concentrations using the membrane-filtration apparatus in Figure S15a, with results presented in Figures S19a-b. The tests were performed for more than a day to ensure a steady state was reached. Figure S19a shows that the permeation rate increased linearly with feed concentration, indicating the presence of the solution-diffusion mechanism.²⁸ In addition, as displayed in Figure S19b, the rejection remained constant with increasing feed concentration, indicating size-exclusion was also at play.²⁹

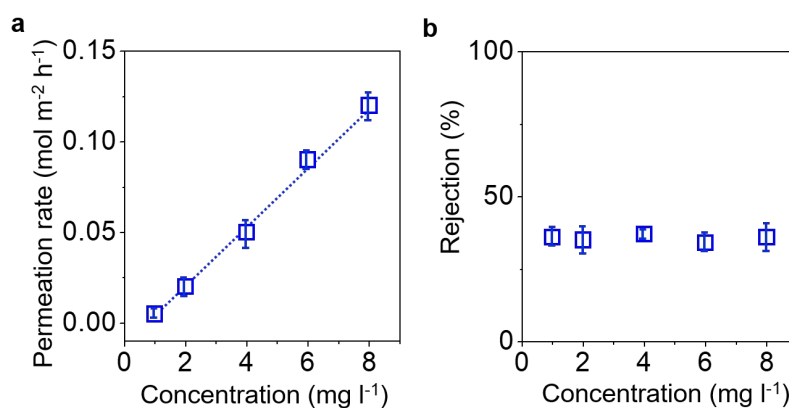


Figure S19. Solute permeation through 97 nm thick NiS₂/NiAILDH membrane: a) Permeation rate and b) rejection of MO solute in acetone solvent with different concentration.

References

- (1) Zhang, C.; Zhao, J.; Zhou, L.; Li, Z.; Shao, M.; Wei, M. Layer-by-layer assembly of exfoliated layered double hydroxide nanosheets for enhanced electrochemical oxidation of water. *J. Mater. Chem. A* **2016**, *4*, 11516-11523.
- (2) Connolly, M. L. Computation of molecular volume. *J. Am. Chem. Soc.* **1985**, *107*, 1118-1124.
- (3) Fei, F.; Cseri, L.; Szekely, G.; Blandford, C. F. Robust covalently cross-linked polybenzimidazole/graphene oxide membranes for high-flux organic solvent nanofiltration. *ACS Appl. Mater. Interfaces* **2018**, *10*, 16140-16147.
- (4) Jimenez Solomon, M. F.; Bhole, Y.; Livingston, A. G. High flux membranes for organic solvent nanofiltration (OSN)—Interfacial polymerization with solvent activation. *J. Membr. Sci.* **2012**, *423-424*, 371-382.
- (5) Siddique, H.; Bhole, Y.; Peeva, L. G.; Livingston, A. G. Pore preserving crosslinkers for polyimide OSN membranes. *J. Membr. Sci.* **2014**, *465*, 138-150.
- (6) da Silva Bural, J.; Peeva, L.; Marchetti, P.; Livingston, A. Controlling molecular weight cut-off of PEEK nanofiltration membranes using a drying method. *J. Membr. Sci.* **2015**, *493*, 524-538.
- (7) Dutczak, S. M.; Cuperus, F. P.; Wessling, M.; Stamatialis, D. F. New crosslinking method of polyamide-imide membranes for potential application in harsh polar aprotic solvents. *Sep. Purif. Technol.* **2013**, *102*, 142-146.
- (8) Kim, I.-C.; Jegal, J.; Lee, K.-H. Effect of aqueous and organic solutions on the performance of polyamide thin-film-composite nanofiltration membranes. *J. Polym. Sci. B: Polym. Phys.* **2002**, *40*, 2151-2163.
- (9) Solomon, M. F. J.; Bhole, Y.; Livingston, A. G. High flux hydrophobic membranes for organic solvent nanofiltration (OSN)—Interfacial polymerization, surface modification and solvent activation. *J. Membr. Sci.* **2013**, *434*, 193-203.
- (10) Solomon, M. F. J.; Song, Q.; Jelfs, K. E.; Munoz-Ibanez, M.; Livingston, A. G. Polymer nanofilms with enhanced microporosity by interfacial polymerization. *Nat. Mater.* **2016**, *15*, 760.
- (11) Jansen, J. C.; Darvishmanesh, S.; Tasselli, F.; Bazzarelli, F.; Bernardo, P.; Tocci, E.; Friess, K.; Randova, A.; Drioli, E.; Van der Bruggen, B. Influence of the blend composition on the properties and separation performance of novel solvent resistant polyphenylsulfone/polyimide nanofiltration membranes. *J. Membr. Sci.* **2013**, *447*, 107-118.
- (12) Li, X.; Fustin, C.-A.; Lefevre, N.; Gohy, J.-F.; Feyter, S. D.; Baerdemaeker, J. D.; Eggere, W.; Vankelecom, I. F. J. Ordered nanoporous membranes based on diblock copolymers with high chemical stability and tunable separation properties. *J. Mater. Chem.* **2010**, *20*, 4333-4339.
- (13) Siddique, H.; Rundquist, E.; Bhole, Y.; Peeva, L. G.; Livingston, A. G. Mixed matrix membranes for organic solvent nanofiltration. *J. Membr. Sci.* **2014**, *452*, 354-366.
- (14) Campbell, J.; Szekely, G.; Davies, R. P.; Braddock, D. C.; Livingston, A. G. Fabrication of hybrid polymer/metal organic framework membranes: mixed matrix membranes versus in situ growth. *J. Mater. Chem. A* **2014**, *2*, 9260-9271.
- (15) Ding, R.; Zhang, H.; Li, Y.; Wang, J.; Shi, B.; Mao, H.; Dang, J.; Liu, J. Graphene oxide-embedded nanocomposite membrane for solvent resistant nanofiltration with enhanced rejection ability. *Chem. Eng. Sci.* **2015**, *138*, 227-238.
- (16) Geens, J.; Boussu, K.; Vandecasteele, C.; Bruggen, B. V. Modelling of solute transport in non-aqueous nanofiltration. *J. Membr. Sci.* **2006**, *281*, 139-148.

- (17) Hosseinabadi, S. R.; Wyns, K.; Meynen, V.; Carleer, R.; Adriaenssens, P.; Buekenhoudt, A.; Bruggen, B. V. Organic solvent nanofiltration with grignard functionalised ceramic nanofiltration membranes. *J. Membr. Sci.* **2014**, *454*, 496-504.
- (18) Ang, H.; Hong, L. Polycationic polymer-regulated assembling of 2D MOF nanosheets for high-performance nanofiltration. *ACS Appl. Mater. & Interfaces* **2017**, *9*, 28079-28088.
- (19) Yang, Q.; Su, Y.; Chi, C.; Cherian, C. T.; Huang, K.; Kravets, V. G.; Wang, F. C.; Zhang, J. C.; Pratt, A.; Grigorenko, A. N.; Guinea, F.; Geim, A. K.; Nair, R. R. Ultrathin graphene-based membrane with precise molecular sieving and ultrafast solvent permeation. *Nat. Mater.* **2017**, *16*, 1198-1202.
- (20) Yeh, C.-N.; Raidongia, K.; Shao, J.; Yang, Q.-H.; Huang, J. On the origin of the stability of graphene oxide membranes in water. *Nat. Chem.* **2015**, *7*, 166.
- (21) Qu, Y.; Zhang, Q. G.; Soyekwo, F.; Gao, R. S.; Lv, R. X.; Lin, C. X.; Chen, M. M.; Zhu, A. M.; Liu, Q. L. Nickel hydroxide nanosheet membranes with fast water and organics transport for molecular separation. *Nanoscale* **2016**, *8*, 18428-18435.
- (22) Ang, H.; Hong, L. Engineering defects into nickel-based nanosheets for enhanced water permeability. *J. Mater. Chem. A* **2017**, *5*, 20598-20602.
- (23) Han, Y.; Xu, Z.; Gao, C. Ultrathin graphene nanofiltration membrane for water purification. *Adv. Funct. Mater.* **2013**, *23*, 3693-3700.
- (24) Schreiber, L.; Schönherr, Jörg. Water and solute permeability of plant cuticles. first edn, (Springer-Verlag Berlin Heidelberg, 2009).
- (25) Abraham, J.; Vasu, K. S.; Williams, C. D.; Gopinadhan, K.; Su, Y.; Cherian, C. T.; Dix, J.; Prestat, E.; Haigh, S. J.; Grigorieva, I. V.; Carbone, P.; Geim, A. K.; Nair, R. R. Tunable sieving of ions using graphene oxide membranes. *Nat. Nanotechnol.* **2017**, *12*, 546.
- (26) Sinnott, R. K.; Coulson, J. M.; Richardson, J. F. Coulson & Richardson's Chemical engineering. fourth edn, Vol. 6 (Oxford: Elsevier Butterworth-Heinemann, 2005).
- (27) Wijmans, J. G.; Baker, R. W. The solution-diffusion model: a review. *J. Membr. Sci.* **1995**, *107*, 1-21.
- (28) Joshi, R. K.; Carbone, P.; Wang, F. C.; Kravets, V. G.; Su, Y.; Grigorieva, I. V.; Wu, H. A.; Geim, A. K.; Nair, R. R. Precise and ultrafast molecular sieving through graphene oxide membrane. *Science* **2014**, *343*, 752-754.
- (29) Krieg, H. M.; Modise, S. J.; Keizer, K.; Neomagus, H. W. J. P. Salt rejection in nanofiltration for single and binary salt mixtures in view of sulphate removal, *Desalination* **2004**, *171*, 205-215.